Eng. Sci., 2025, **38**, 1880

Engineered Science
DOI: https://dx.doi.org/10.30919/es1880

Effect of Mineralizers on the Preparation and Chromatic Properties of Cerium/Praseodymium Co-doped Yellow Ceramic Pigments

Jiang Feng,[1,*] Jie Liu,[1] Junxiong Zhang,[1] Zhibin Chen,[1] Guo Feng,[2] Quan Zhang,[2] Xiaojun Zhang[2] and Jianmin Liu[2]

Abstract

To address the shortcomings of traditional Pr-$ZrSiO_4$ yellow ceramic pigments, including their cool tone, empirical mineralizer selection, and inefficiencies in energy consumption and yield, this study synthesized (Ce, Pr)-$ZrSiO_4$ pigments using a mechanochemical-assisted molten salt method at 900 °C. Three fluoride mineralizers (LiF, MgF_2, NaF) were systematically compared. Results show NaF exhibited optimal mineralization and the ability to promote chromogenic development due to the similar ionic radii of Na^+ and Pr^{3+}, enabling a Pr^{3+}-Na^+ co-occupancy mechanism that effectively compensates for the charge imbalance from Pr^{3+} substituting for Zr^{4+}, thereby increasing the content of the chromogenic Pr^{4+} species. With an optimized F/Zr molar ratio of 0.3, a well-crystallized warm-yellow pigment was obtained ($L^* = 80.29$, $a^* = 5.42$, $b^* = 68.39$). This research not only optimized the color performance of (Ce, Pr)-$ZrSiO_4$ pigments but also revealed the underlying mechanism of Pr^{3+}-Na^+ co-occupancy, providing an important theoretical basis and an optimized process scheme for the preparation of this type of traditional pigment.

Keywords: Yellow ceramic pigment; Mineralizer; Co-occupancy; Mechanochemical-assisted molten salt method.
Received: 20 July 2025; Revised: 15 October 2025; Accepted: 24 October 2025
Article type: Research article.

1. Introduction

In the field of ceramic decoration, yellow pigments have always held significant importance. Early traditional varieties that were widely used included vanadium-zirconium yellow, tin-vanadium yellow, cadmium yellow, and lead-antimony yellow. It was not until the 1950s and 1960s, with the development of rare earth chemistry, that zircon based ceramic pigments began to be widely applied in commercial production.[1,2] With the continuous deepening of research on zircon based ceramic pigments, researchers have been constantly optimizing their synthesis methods and color performance. Currently, the main synthesis methods for zircon based pigments include the molten salt method, solid-state method, sol-gel method, and chemical precipitation method. The conventional molten salt method requires the pre-addition of salt. However, the added salt may cause localized reaction heterogeneity due to uneven physical mixing and can easily introduce additional impurities.[3] The solid-state synthesis method forms the crystalline phase through a solid-solid diffusion reaction between ZrO_2 and SiO_2, but its reaction temperature needs to be maintained above 1300 °C, significantly increasing energy consumption costs.[4] As an improved process, the sol-gel method can significantly reduce the synthesis temperature.[5] However, its complex optimization of sol precursor ratios and low yield still restrict the progress of industrial mass production. In contrast, the chemical precipitation method holds advantages in process simplicity and product particle size control, enabling the preparation of nano-sized pigment particles.[6] Nevertheless, this method faces problems such as unstable color performance and a tendency to generate by-products. Meanwhile, the wastewater produced during the reaction requires the configuration of specialized treatment systems to meet environmental protection requirements.

To overcome the aforementioned limitations, this study proposes a mechanochemical-assisted molten salt method. This approach uses hydrated Lewis acid ($ZrOCl_2 \cdot 8H_2O$) and

---

[1] *School of Material Science and Engineering, Jingdezhen Ceramic University, Jingdezhen, Jiangxi, 333403, China*
[2] *National Engineering Research Center for Domestic and Building Ceramics, Jingdezhen, Jiangxi, 333001, China*
[*] *Email:* jiangfeng@jcu.edu.cn (F. Jiang)

Table 1: Reagent information.

Reagent	Molecular formula	Purity	Manufacturer
Zirconyl Chloride Octahydrate	$ZrOCl_2·8H_2O$	AR	Shanghai Aladdin Co., Ltd.
Sodium Metasilicate Nonahydrate	$Na_2SiO_3·9H_2O$	AR	Shanghai Aladdin Co., Ltd.
Praseodymium Chloride Hexahydrate	$PrCl_3·6H_2O$	AR	Shanghai Macklin Co., Ltd.
Cerium Chloride Heptahydrate	$CeCl_3·7H_2O$	AR	Shanghai Aladdin Co., Ltd.
Lithium Fluoride	LiF	CP	Sinopharm Chemical Reagent Co., Ltd.
Magnesium Fluoride	MgF_2	CP	Sinopharm Chemical Reagent Co., Ltd.
Sodium Fluoride	NaF	CP	Sinopharm Chemical Reagent Co., Ltd.
Transparent Glaze	/	/	Jiangxi Peiyintang Ceramic Glaze Co., Ltd.

Lewis base ($Na_2SiO_3·9H_2O$) as the main raw materials. During the mechanical milling process, the effects of shearing, friction, impact, and compression facilitate the activation and homogeneous mixing of the reactants at room temperature.[7] A neutralization reaction occurs between them during mechanical treatment, releasing water into the reaction system. This released water not only accelerates the reaction rate but also acts as a "micro-solvent," providing a liquid phase environment that further promotes ion migration and component diffusion, thereby ensuring high chemical homogeneity in the precursor. Simultaneously, NaCl molten salt is generated in situ, creating an environmentally friendly and low-cost intrinsic molten salt environment. This environment ensures the close contact of reactants at the molecular scale, enabling the uniform distribution of the zirconium source, silicon source, chromogenic ions, and doping ions.

In this system, the introduction of mineralizers plays a key role in the formation of the zircon crystal phase and the color presentation of the pigment. Since it was confirmed that fluorides can serve as effective mineralizers for synthesizing zirconium-praseodymium yellow pigments, this field has continued to receive extensive attention.[8] It is widely accepted that mineralizers improve the color development of $Pr\text{-}ZrSiO_4$ yellow pigments by promoting the formation of the zircon crystal phase.[9] It is worth noting that this study found that in the (Ce, Pr)-$ZrSiO_4$ co-doping system, the role of mineralizers surpasses traditional understanding: they not only promote the mass transfer process through F^- ions, but their cations can also directly participate in the charge compensation process. This discovery is particularly important for controlling the color presentation of the pigment. Furthermore, traditional zirconium-praseodymium yellow pigments generally exhibit a cool tone with a slight greenish tint,[4-6] while the introduction of Ce ions can effectively adjust the tone from cool to warm orange-yellow.[10] However, existing research mostly focuses on the effects of parameters such as Ce/Pr doping ratio and synthesis temperature, while the mechanism of mineralizers in this co-doping system, especially the key role of their cations in charge compensation, still lacks systematic research.[9,11,12]

To systematically reveal the influence of cation charge compensation capability on the phase composition, microstructure, and color performance of (Ce, Pr)-$ZrSiO_4$ pigments, this study designed a comparative system, selecting LiF (+1 valence, $^{[VIII]}Li^+$ (r = 0.92 Å)), MgF_2 (+2 valence, $^{[VIII]}Mg^{2+}$ (r = 0.89 Å)), and NaF (+1 valence, $^{[VIII]}Na^+$ (r = 1.18 Å)) as mineralizers.[13] This design aims to verify the following scientific hypothesis: in this system where external fluorides mineralizer and intrinsic NaCl molten salt coexist, whether Na^+, by virtue of its excellent compatibility derived from sharing the same cation type with the molten salt medium and its similar ionic radius to Pr^{3+}, can achieve superior charge compensation effects compared to Li^+ or Mg^{2+} through an efficient co-occupancy mechanism, thereby obtaining better mineralization effect and color performance.

2. Materials and methods

2.1 Synthesis of (Ce, Pr)-$ZrSiO_4$ pigments

In this study, high color performance cerium and praseodymium co-doped zircon based yellow ceramic pigments with low Pr content were synthesized by mechanochemical-assisted molten salt method. The specific experimental procedure was as follows: According to the stoichiometric ratio, 10 mmol of $ZrOCl_2·8H_2O$ and $Na_2SiO_3·9H_2O$ were weighed as the zirconium and silicon sources, with 0.5 mmol of $PrCl_3·6H_2O$ and 0.7 mmol of $CeCl_3·7H_2O$ added as chromogenic and doping ions. Additionally, 2 mmol of LiF, 2 mmol of NaF, and 1 mmol of MgF_2 were introduced (ensuring not only a constant total amount of fluoride ions but also an equal total positive charge from the mineralizer cations in the system). The information of reagents used is provided in Table 1. All raw materials were ground in an agate mortar for 0.5 h to form a paste-like mixture, which was then dried at 60 °C for 2 h to obtain the precursor. The precursor was placed in a corundum crucible and calcined at 900 °C for 3 h. The calcined product was washed with deionized water, dried at 60 °C for 6 h, and the final pigment sample was obtained. A flowchart of the pigment preparation process is shown in Fig. 1. To evaluate the pigment performance, the obtained pigment was mixed into a commercial transparent glaze at 5 wt%, and enameled samples were prepared by calcining at 1200 °C for 0.5 h. The chemical composition of the transparent glaze is provided in Table 2.

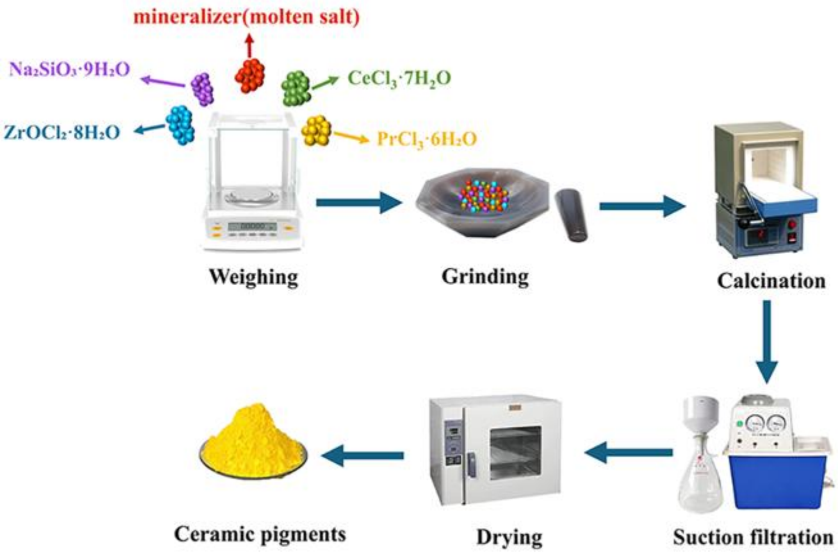

Fig. 1: Experimental process schematic diagram.

Table 2: Chemical composition of transparent glaze.

Chemical composition	Content (wt.%)	Chemical composition	Content (wt.%)
SiO_2	58.64	K_2O	1.24
Al_2O_3	8.61	MgO	0.21
CaO	10.16	ZnO	5.37
Na_2O	4.82	else	0.89
BaO	1.62	IL	8.44

2.2 Characterization

The crystalline phase composition of the pigment samples was analyzed by X-ray diffractometer (XRD, D8 Advance, Bruker, Germany). Data were collected over the 2θ range of 10°–70° with a scan rate of 0.02°/s. Rietveld refinements were performed using the GSAS software, and the experimental data were collected in the 5–90° 2θ angular range with a step 0.02° (2θ/s) and counting time 4 s.[14] The thermal decomposition behavior of the precursor was studied by differential thermal analysis and thermogravimetric (DTA-TG, STA 449C, Netzsch, Germany) in air with a heating rate of 10 °C min^{-1}. Microstructure characterization was carried out by field-emission scanning electron microscopy (FE-SEM, SU-8010, Hitachi, Japan) equipped with an energy-dispersive X-ray spectroscopy (EDS) system. Lattice distortion within the pigment powder was analyzed by transmission electron microscopy (TEM, JEM-F200, Jeol, Japan). The chemical valence states of constituent elements were investigated by X-ray photoelectron spectroscopy (XPS, ESCALAB 250XI, Thermo-Scientific, America). The diffuse reflectance spectra of the pigment powder were recorded using a UV-Vis spectrophotometer (Lambda850, PerkinElmer, America). The CIE $L^*a^*b^*$ color parameters of the samples were measured with an automatic whiteness meter (WSD-3C, Kang Guang, China). The L^* value represents lightness, ranging from 0 (black) to 100 (white). The a^* value denotes the red (+) to green (−) axis, and the b^* value denotes the yellow (+) to blue (−) axis. The particle size distribution information of the pigment powder was obtained using a laser particle size analyzer (Mastersizer 3000, Malvern, England).

3. Results and discussion

3.1 Precursor characterization and thermal behavior analysis

Fig. 2(a) shows the XRD patterns of the precursors of three pigment samples with different mineralizers after grinding and before calcination. The corresponding TG-DTA curves for these pigment samples are shown in Fig. 2(b), (c), and (d). As observed from Fig. 2(a), diffraction peaks corresponding to NaCl (JCPDS No. 05-0628) were detected following grinding, consistent with the reaction shown in Eq. (1).[15]

$$ZrOCl_2{\cdot}8H_2O + Na_2SiO_3{\cdot}9H_2O \rightarrow ZrO_2\,(\text{amorphous}) + SiO_2(\text{amorphous}) + 2NaCl + 17H_2O \quad (1)$$

Prior literature has established NaCl as an environmentally benign and cost-effective molten salt for ceramic pigment synthesis.[16] As evident in Fig. 2(b)-(d), Exothermic peaks are observed in the DTA curves of the three pigment samples at 632.1 °C (LiF), 673.2 °C (MgF_2), and 667.3 °C (NaF). As reported previously,[17] these exothermic peaks are confirmed to result from phase transformations in zirconia and cristobalite occurring between 600 °C and 700 °C, with no significant mass loss observed in the corresponding TG curves. Furthermore, the DTA curves revealed three distinct endothermic peaks for three pigment samples at other positions: the sample with added LiF (Fig. 2(b)) showed peaks at 120.0 °C, 763.2 °C, and 1093.0 °C; the sample with added MgF_2 (Fig. 2(c)) showed peaks at 112.1 °C, 790.8 °C, and 1078.0 °C; and the sample with added NaF (Fig. 2(d)) showed

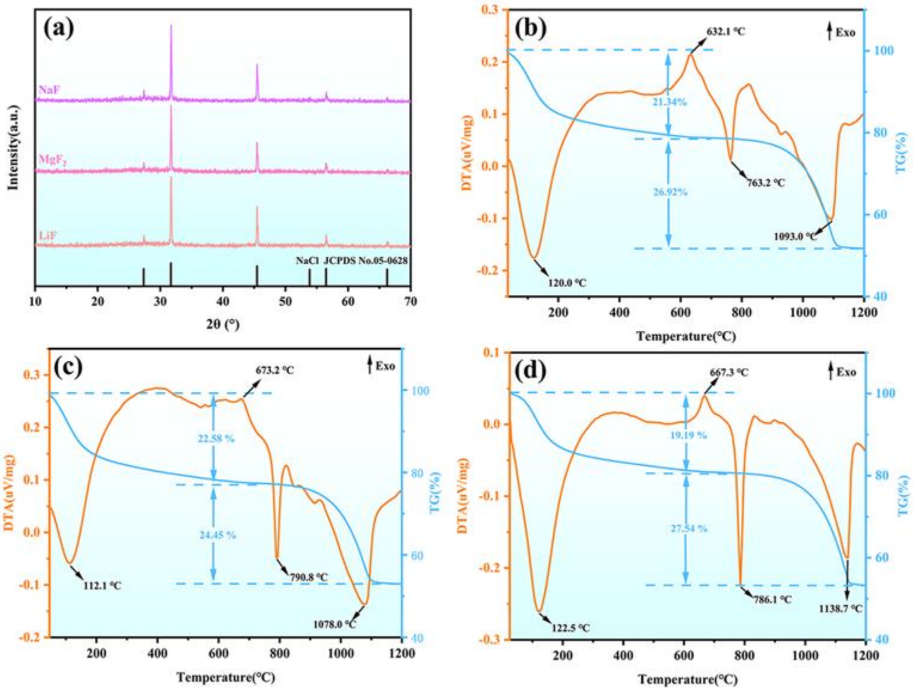

Fig. 2: (a) XRD patterns of the precursors of three pigment samples with different mineralizers after grinding and before calcination; TG-DTA curves of pigment samples: (b) LiF; (c) MgF_2; (d) NaF.

peaks at 122.5 °C, 786.1 °C, and 1138.7 °C. Specifically, the endothermic peaks at 120.0 °C (LiF), 112.1 °C (MgF_2), and 122.5 °C (NaF), along with their corresponding mass loss in the TG curves, are attributed to the evaporation of crystalline water, the sharp endothermic peaks observed at 763.2 °C (LiF), 790.8 °C (MgF_2), and 786.1 °C (NaF) correspond to the melting of mixtures containing *in-situ* formed NaCl and fluoride mineralizers,[18-20] the endothermic peaks at 1093.0 °C (LiF), 1078.0 °C (MgF_2), and 1138.7 °C (NaF), which are accompanied by mass loss in the respective TG curves, are linked to material volatilization.[21]

3.2 Effect of different fluoride mineralizers on (Ce, Pr)-$ZrSiO_4$ pigments

Fig. 3 shows the XRD patterns of pigment samples synthesized with different fluoride mineralizers. The patterns indicate that the main crystalline phase in all three pigment samples is zircon, with sharp diffraction peaks confirming their well-crystallized nature. This suggests that LiF, MgF_2, and NaF exert a significant mineralization effect, effectively reducing the activation energy barrier for the zircon synthesis reaction and promoting its crystallization.[22] However, unreacted ZrO_2 and SiO_2 residues are present in the LiF and MgF_2 prepared samples. In contrast, only ZrO_2 residues were detected in the NaF prepared sample. This observation suggests that, under the given experimental conditions, NaF exhibits superior mineralizing effectiveness compared to LiF and MgF_2.

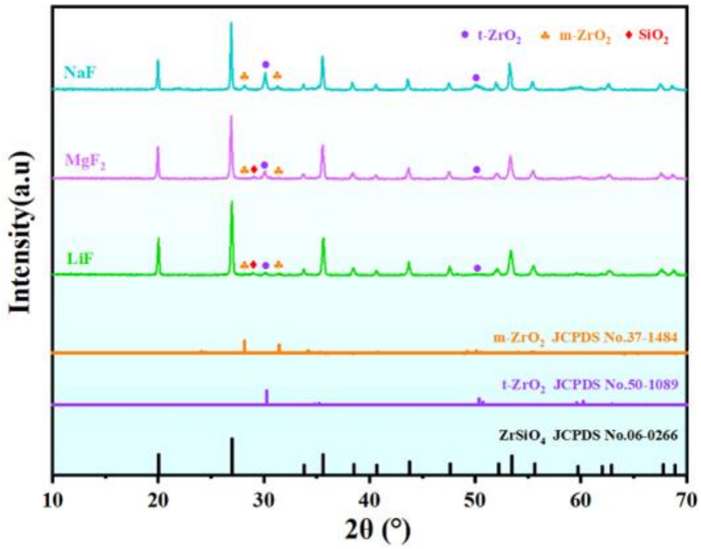

Fig. 3: XRD patterns of pigment samples prepared with different fluoride mineralizers.

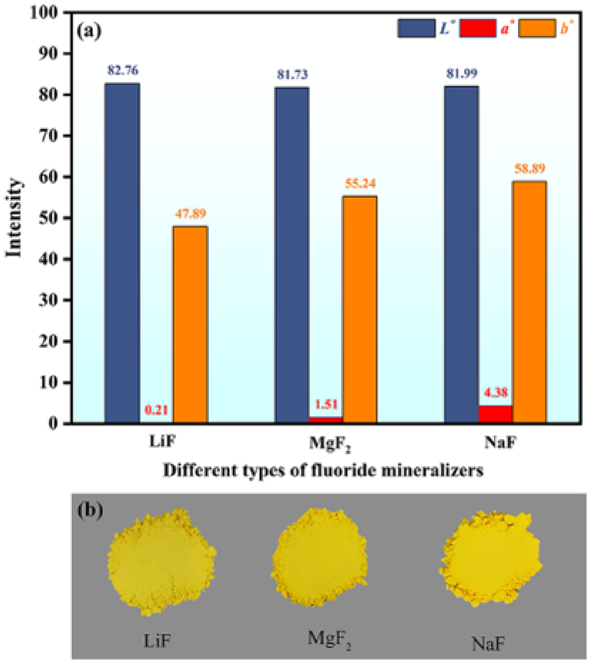

Fig. 4: Pigment samples prepared with different fluoride mineralizers; (a) CIE $L^*a^*b^*$ *values*, (b) digital photographs.

Fig. 4 presents the L^*, a^*, b^* values and digital photographs of pigment samples prepared with different mineralizers. The pigments synthesized with LiF, MgF_2, and NaF as mineralizers all exhibit a bright yellow coloration. The L^* values show little change, while both a^* and b^* values display an increasing trend. The sample adding NaF showed the most excellent color performance (b^* = 58.89), this finding is consistent with the previous inference. To further investigate the reason why the pigment sample with NaF as the mineralizer exhibited the optimal color performance, the following characterization tests and Rietveld refinement of XRD data were performed on pigment samples prepared with the three mineralizers (LiF, MgF_2, NaF).

Fig. 5 shows the SEM images of pigment samples synthesized using different fluoride mineralizers, corresponding to samples prepared with LiF, MgF_2, and NaF as mineralizers, respectively. It can be observed from the figures that the type of mineralizer has a significant influence on the morphology, size, and aggregation behavior of the pigment particles. The pigment particles of the sample with LiF added are small tetragonal bipyramidal grains with a particle size distribution between 1-2 µm, showing obvious aggregation and forming large aggregates. The pigment particles of the sample with MgF_2 added all exhibit short columnar tetragonal bipyramidal grains with a particle size distribution between 1-3 µm; the degree of aggregation is lighter, and particle dispersibility is relatively better. The pigment particles of the sample with NaF added show well-developed elongated columnar tetragonal bipyramidal morphology with larger particle sizes, ranging between 1-6 µm. There is minor localized aggregation between grains, but the crystal morphology is complete with clear edges and corners, indicating that NaF promotes directional crystal growth. The reason for the aforementioned phenomena is related to the reactivity of the mineralizers, with fluoride ions being the key component that promotes the synthesis of zircon. At certain temperatures, the mineralizer and the raw materials undergo the following reaction (taking NaF as an example, the corresponding reaction is shown in Eq. (2)-(4)):[23]

$$NaF + SiO_2 \rightarrow SiF_4\uparrow + Na_2O \tag{2}$$

$$SiF_4 + ZrO_2 + O_2 \rightarrow ZrSiO_4 + F_2\uparrow \tag{3}$$

$$F_2 + SiO_2 \rightarrow SiF_4\uparrow + O_2\uparrow \tag{4}$$

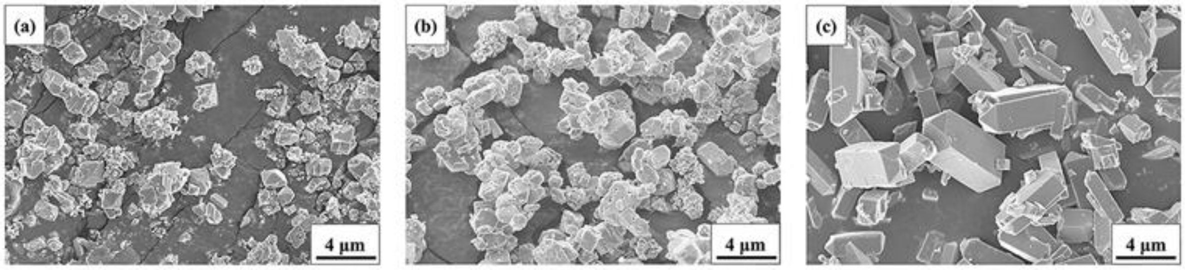

Fig. 5: FE-SEM images of pigment samples with different fluoride mineralizers: (a) LiF; (b) MgF_2; (c) NaF.

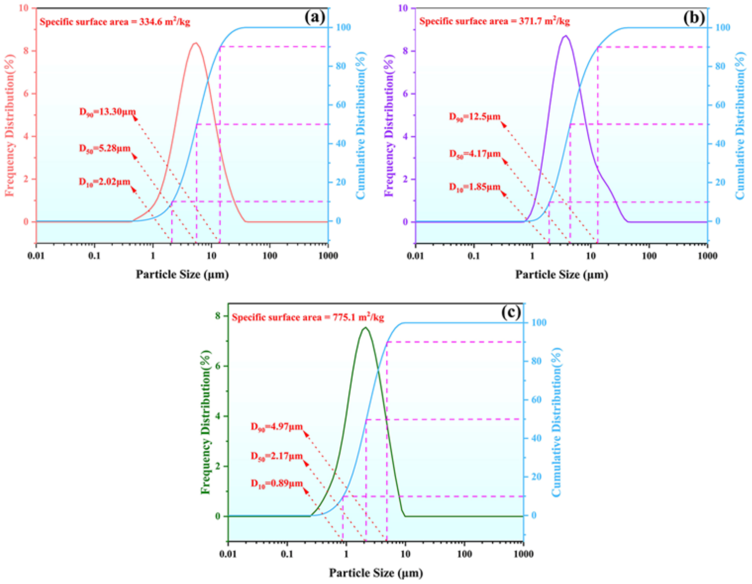

Fig. 6: Particle size distribution of pigment samples prepared with different fluoride fluxes: (a) LiF, (b) MgF_2, (c) NaF.

The mineralization effect of the fluorides used in this experiment is mainly reflected in Eq. (2), i.e., the different generation rates of SiF_4.[24] Among the three mineralizers—LiF, MgF_2, and NaF—LiF exhibits the strongest reactivity. This is because Li^+ has an electronegativity of 1.0, which gives it a stronger attraction to O^{2-} than Si^{4+}.[25] At high temperatures, LiF readily breaks the Si–O–Si bonds, thereby generating a large amount of SiF_4 gas. This gas creates a highly supersaturated concentration environment, and since the nucleation rate of $ZrSiO_4$ crystals is positively correlated with the degree of supersaturation, it consequently leads to the formation of a large number of $ZrSiO_4$ crystal nuclei. Meanwhile, the low eutectic point liquid phase formed by LiF-NaCl (approximately 763.2 °C) enhances the dispersion of reactants, further increasing the number of effective nucleation sites. Due to the high density of crystal nuclei, the distances between nuclei become very close. As a result, the crystal nuclei exhibit a competitive growth trend, which limits the growth of each nucleus and prevents them from developing into large-sized grains. Ultimately, fine tetragonal bipyramidal grains with high surface energy are formed. However, the high surface energy drives the particles to agglomerate in order to reduce the system energy, thus leading to the significant agglomeration observed in the LiF sample.[26] In contrast, MgF_2 and NaF have relatively lower reactivity compared to LiF, resulting in slower SiF_4 generation rates and milder reaction conditions. The lower nucleation rate leads to a smaller total number of crystal nuclei, allowing each nucleus to receive a sufficient and sustained supply of growth substances from the environment. Therefore, this ultimately promotes the development of columnar crystals.[27]

To further accurately evaluate the overall particle size distribution and average particle size of the pigment samples, thereby compensating for the limitation of FE-SEM which only observes morphology in localized areas, this study employed a laser particle size analyzer to test and analyze pigment samples prepared with different fluoride mineralizers. Fig. 6 shows the particle size distribution of pigment particles under different fluoride mineralizer conditions. From Fig. 6 (a-c), it can be seen that the pigment particles prepared by mechanochemical-assisted molten salt method all have small particle sizes, with D_{90} values all less than 14 μm. Among these samples, the pigment sample with NaF added (corresponding to Fig. 6(c)) exhibited the most optimal particle size distribution characteristics. It's D_{10}, D_{50}, and D_{90} values were 0.89 μm, 2.17 μm, and 4.97 μm, respectively, all being the smallest among the three. Combining with Fig. 4, although the particles of pigments synthesized with LiF and MgF_2 are smaller in size, their severe agglomeration leads to poorer particle size distribution.

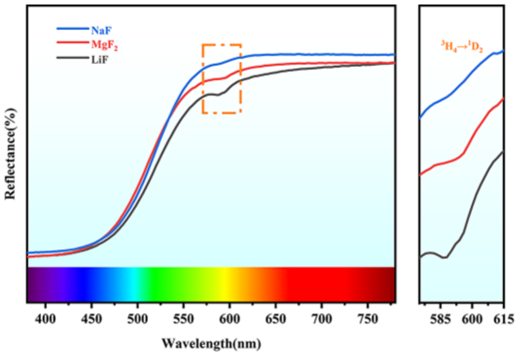

Fig. 7: UV-Vis spectra of pigment samples prepared with different fluoride mineralizers.

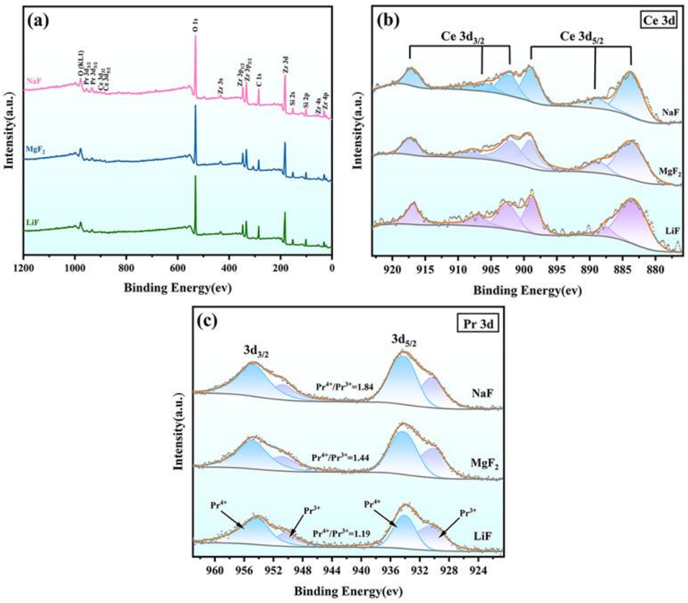

Fig. 8: Pigment samples prepared with different fluoride mineralizers: (a) XPS spectra; (b) high resolution spectra of Ce 3d; (c) high resolution spectra of Pr 3d.

Fig. 7 displays the UV-Vis spectra of pigment samples prepared with different fluoride mineralizers. All spectra exhibit a gradual increase in reflectance across the wavelength range of 380-780 nm. The sample adding NaF demonstrates the highest reflectance, corresponding to the most intense yellow hue. Furthermore, an absorption band is observed near 590 nm. This band is attributed to the $^3H_4 \rightarrow {}^1D_2$ electronic transition within the 4f orbitals of Pr^{3+} cations.[12] As this absorption peak lies within the spectral region of high yellow reflectance, it detrimentally affects color development. In contrast, the sample with added NaF pigment exhibits the weakest absorption band intensity among the samples, resulting in a higher yellowness index. This spectroscopic behavior aligns well with the observed color characteristics.

Fig. 8 presents the XPS spectra of pigment samples synthesized with different mineralizers. As discerned from Fig. 8(a), the sample comprises the elements Zr, Si, O, Pr, Ce, Na, and C. with the carbon signal originating from the reference standard.

Discovered through high-resolution spectroscopy, six distinct peaks are observed in the Ce 3d XPS spectrum (Fig. 8(b)) at binding energies of 916.7, 906.9, 902.4, 898.7, 887.4, and 883.3 eV. As reported,[28] the peaks at 883.3 eV and 902.4 eV are assigned to the binding energies of Ce $3d_{5/2}$ and Ce $3d_{3/2}$, respectively. The dominant peaks at 916.7 eV and 898.7 eV correspond to the $3d^{10}4f^0$ initial electronic state characteristic of Ce^{4+}. Meanwhile, the peaks at 883.3, 887.4 eV and 902.4, 906.9 eV are attributed to hybridized final states involving $3d^94f^2$ and $3d^94f^1$ configurations;[29] no peaks attributable to Ce^{3+} are detected. Consequently, the doped Ce in the pigment particles exists exclusively in the +4 state. The Pr 3d XPS spectrum (Fig. 8(c)) exhibits four distinct peaks positioned at approximately 953.9, 950.4, 934.1, and 929.9 eV. From the literature known so far,[30,31] the Characteristic Peaks near 954.4 eV and 934.1 eV correspond to tetravalent praseodymium cations (Pr^{4+}), while those near 950.4 eV and 929.9 eV are characteristic of trivalent praseodymium cations (Pr^{3+}). Collectively, these findings confirm the coexistence of Pr cations in two distinct states ($Pr^{4+}$and Pr^{3+}) alongside Ce^{4+} within the zircon based pigment system.

Semi-quantitative calculation of the Pr^{4+}/Pr^{3+} molar ratio using Avantage software yielded values of 1.19, 1.44, and 1.84 for pigments containing LiF, MgF_2, and NaF mineralizers, respectively. As the coloring mechanism of praseodymium zircon yellow pigments involves Pr^{4+} doped into the zircon structure inducing lattice distortion, thus a higher Pr^{4+}/Pr^{3+} molar ratio facilitates improved coloring performance.[29] Based on these calculated results, the NaF-mineralized pigment sample exhibits optimal color performance, demonstrating excellent consistency with experimental findings.

Given that the pigments synthesized with the three mineralizers exhibit significant differences in color performance (Fig. 4) under the same total molar amount of fluoride ions, this indicates that the type of cation in the mineralizers also plays an important role in the color properties of the pigments. To explain the notable influence of different mineralizers on pigment performance, we propose a charge compensation mechanism via cation co-occupancy governed by ionic radius matching. The core of this mechanism lies in the fact that mineralizer cations (*e.g.*, Na^+) and Pr^{3+}, due to their similar ionic radii, can cooperatively enter the crystal lattice and achieve synergistic substitution of lattice sites. This radius matching is the key factor in reducing lattice distortion, achieving efficient charge compensation, and stabilizing the Pr^{4+} chromogenic center.

During the high-temperature synthesis process, Pr is typically introduced in the form of Pr^{3+}, which ultimately needs to be oxidized to substitute for Zr^{4+} in the $ZrSiO_4$ lattice, thereby forming the chromogenic Pr^{4+}. This substitution process ($Pr^{3+} \rightarrow Zr^{4+}$) leads to a local imbalance of one unit of negative charge, thus hindering the effective doping of Pr ions. To restore charge balance, the cations from the mineralizers (*e.g.*, Li^+, Mg^{2+}, Na^+) must provide charge compensation. Unlike entering interstitial sites, this study proposes that these cations are more likely to directly occupy the sites of zirconium vacancies ($V_{Zr}^{''''}$) generated by the charge imbalance. Here, we take the NaF mineralizer as an example to provide a detailed explanation. The model is based on the high degree of matching between their ionic radii ($^{[VIII]}Pr^{3+}$ (r = 1.126 Å), $^{[VIII]}Na^+$ (r = 1.18 Å), $^{[VIII]}Zr^{4+}$ (r = 0.84 Å)).[13] One Pr^{3+} ion and one Na^+ ion can co-enter the lattice, and this co-occupancy can be expressed by the following defect reaction show in Eq. (5)

$$Pr^{3+} + Na^{+} \xrightarrow{ZrSiO_4} Pr_{Zr}^{'} + Na_{Zr}^{'''} \tag{5}$$

In this process, the single positive charge carried by Na+ precisely compensates for the single negative charge imbalance introduced by the substitution of Pr^{3+} for Zr^{4+}, achieving effective local charge balance. More importantly, the similar ionic radii of Pr^{3+} and Na^+ result in significantly less lattice distortion from this cooperative substitution compared to their individual substitutions, making it thermodynamically more favorable. This Pr^{3+}-Na^+ co-occupancy unit not only provides a stable initial environment for Pr^{3+} doping but also establishes a locally charge-neutral structure that creates a stable crystal field environment for the subsequent oxidation of Pr^{3+} to Pr^{4+}. However, as shown in Fig. 8(c), not all Pr^{3+} ions are oxidized to Pr^{4+}, and a certain amount of residual Pr^{3+} always remains in the system. In such cases, these Na+ ions still can continue to provide sustained and effective charge compensation for the residual Pr^{3+} through the co-occupancy mechanism, ensuring these ions remain stably incorporated within the lattice without being expelled due to charge imbalance or forming secondary phases. To validate this mechanism, Rietveld refinement of XRD data from samples prepared with different mineralizers was performed to obtain more direct evidence.

Table 3 presents the Rietveld refinement results of XRD data for pigment samples prepared with different fluoride mineralizers. The corresponding parameters (χ^2, Rwp, Rp) all fall within acceptable ranges, indicating the reliability of the refinement models and the credibility of the results. Compared with standard $ZrSiO_4$ (JCPDS No. 06-0266), all samples exhibit varying degrees of unit cell expansion. This phenomenon confirms the successful incorporation of foreign ions (Pr ions and mineralizer cations) into the $ZrSiO_4$ lattice. The extent of lattice expansion differs significantly depending on the mineralizer used. The sample with NaF addition shows the most pronounced expansion in unit cell parameters (a = b = 6.638 Å, c = 6.000 Å) and volume (264.38 Å^3), while samples with LiF and MgF_2 exhibit relatively smaller expansions. This result is highly consistent with the "cation co-occupancy mechanism governed by ionic radius matching" proposed in this study. According to this mechanism, $^{[VIII]}Na^+$ (r = 1.18 Å), due to its close radius matching with $^{[VIII]}Pr^{3+}$ (r = 1.126 Å), can enter the $^{[VIII]}Zr^{4+}$ (r = 0.84 Å) sites through the co-occupancy mechanism described in Eq. (5). In contrast, although the ionic radius of $^{[VIII]}Li^+$ (r = 0.92 Å) is relatively close to that of Zr^{4+}, it is significantly smaller than that of Pr^{3+}. This dimensional mismatch makes the Pr^{3+}-Li^+ co-occupancy geometrically unfavorable, causing Li^+ to tend to occupy interstitial sites.[11] For MgF_2, despite the ionic radius of $^{[VIII]}Mg^{2+}$ (r = 0.89 Å) being similar to that of Zr^{4+}, its divalent positive charge introduces new charge imbalance when compensating for the monovalent negative charge generated by the substitution of Pr^{3+} for Zr^{4+} (one Mg^{2+} compensation would result in one unit of excess positive charge). This makes the stable occupancy of Zr sites by Mg^{2+} more difficult, similarly limiting its effective incorporation into the crystal lattice. Furthermore, according to the quantitative phase analysis results in Table 3, the content of the main crystalline phase (Phase 1) of $ZrSiO_4$ in the NaF-added sample (78.94 wt%) is significantly lower than that in the LiF-added (94.26 wt%) and MgF_2-added (90.99 wt%) samples, while its impurity phases (Phase 2 and Phase 3) show the highest content. This precisely indicates that NaF, through its efficient co-occupancy mechanism, maximizes the incorporation of Pr ions. In contrast, due to the lower charge compensation efficiency of LiF and MgF_2, more Pr ions fail to enter the zircon lattice or remain predominantly in the form of Pr^{3+}, ultimately resulting in inferior color performance.

Table 3: Rietveld refinement results for pigment samples prepared with different fluoride mineralizers.

samples	LiF	MgF_2	NaF	JCPDS No. 06-0266
a=b (Å)	6.630	6.630	6.638	6.604
c (Å)	5.995	5.997	6.000	5.979
$\alpha = \beta = \gamma$ (°)	90.0	90.0	90.0	90.0
volume (Å^3)	263.58	263.68	264.38	260.80
Phase 1 (wt%)	94.26	90.99	78.94	/
Phase 2 (wt%)	3.38	1.71	5.38	/
Phase 3 (wt%)	2.36	7.30	15.68	/
χ^2	4.38	4.51	6.45	/
R_{wp} (%)	11.52	11.64	8.84	/
R_p (%)	8.36	8.44	6.23	/

Note: Phase 1: $ZrSiO_4$, Phase 2: m-ZrO_2, Phase 3: t-ZrO_2.

Based on the aforementioned research, it can be concluded that mineralizers play a crucial role in the synthesis of cerium and praseodymium co-doped zircon based yellow ceramic pigments. They not only significantly promote the synthesis and crystal growth of the $ZrSiO_4$ crystalline phase through the formation of active gaseous components (*e.g.*, SiF_4) and liquid media, but more importantly, the type and amount of mineralizer directly affect the doping efficiency, valence state distribution, and local charge balance of the chromogenic ions in the lattice, thereby determining the final color performance of the pigments. This study has confirmed that under the condition of an equivalent fluoride ion amount, NaF, due to the optimal ionic radius match between the introduced Na+ and Pr^{3+}, effectively promotes the formation of the Pr^{4+} chromogenic center through the Pr^{3+}-Na^{+} co-occupancy mechanism. Its overall mineralization effect is superior to that of LiF and MgF_2. However, under the preliminary condition of a fixed addition of 2 mmol NaF, there remains significant room for improvement in the pigment's performance. XRD and refinement results indicate that the sample still contains a relatively high content of m-ZrO_2 and t-ZrO_2 impurity phases, and the content of the main crystalline phase $ZrSiO_4$ is relatively low, suggesting that the reaction is not yet complete and the degree of crystallization needs further enhancement. Correspondingly, the chromaticity parameter b^* value of the pigment powder is 58.89. Although a distinct yellow hue is observed, its color performance still shows a considerable gap compared to the color intensity reported in the literature. Therefore, to fully explore the capability of NaF as a highly effective mineralizer, this study subsequently further optimized the NaF addition amount (F/Zr molar ratio from 0.1 to 0.5), aiming to obtain yellow ceramic pigments with high phase purity and superior color performance.

Fig. 9 shows the XRD patterns of samples prepared with different NaF addition amounts (marked as F/Zr molar ratios from 0.1 to 0.5). At F/Zr = 0.1, the main crystalline phase ZrO_2, accompanied by minor SiO_2 phases, no zircon phase is observed. According to relevant reports,[19] when the amount of NaF added is small, the mineralization effect is insufficient, and increasing the calcination temperature is necessary to form the zircon phase. With increasing NaF addition, the main crystalline phase of the samples transitions to zircon ($ZrSiO_4$, JCPDS No. 06–0266). In the magnified region of 26.5°–27.5°, it can be observed that the position of the strongest diffraction peak shifts toward lower angles.

According to the Bragg equation,[32] the shift of the highest diffraction peak toward lower angles indicates that the formation of (Ce, Pr)-$ZrSiO_4$ is caused by the substitution of smaller-radius ions by larger-radius ions. The relevant ionic radii in this system are $^{[VIII]}Pr^{3+}$ (r = 1.126 Å), $^{[VIII]}Pr^{4+}$ (r = 0.96 Å), $^{[VIII]}Ce^{4+}$ (r = 0.97 Å), and $^{[VIII]}Zr^{4+}$ (r = 0.84 Å).[13] Simultaneously, the intensity of the diffraction peaks of the zirconium oxide impurity phases decreases significantly, indicating that an appropriate amount of NaF effectively promotes the formation of the zircon phase. When F/Zr = 0.3, the XRD pattern of the sample displays the sharpest and highest-intensity $ZrSiO_4$ diffraction peaks, indicating optimal crystallinity. To obtain more precise phase composition and structural information, we performed XRD Rietveld refinement on this sample.

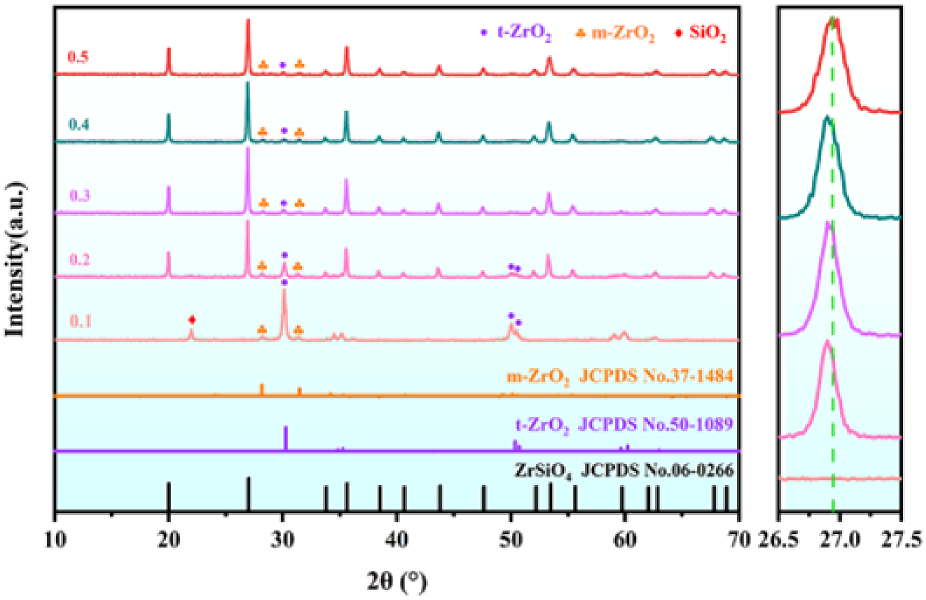

Fig. 9: XRD patterns of pigment samples prepared with different amounts of NaF mineralizer.

Table 4: Rietveld refinement result of the pigment sample at F/Zr = 0.3.

a=b (Å)	c (Å)	$\alpha=\beta=\gamma$ (°)	volume (Å^3)	Phase 1 (wt%)	Phase 2 (wt%)	Phase 3 (wt%)	χ^2	R_{wp} (%)	R_p (%)
6.639	6.002	90	264.55	90.39	3.97	5.81	2.04	8.48	6.44

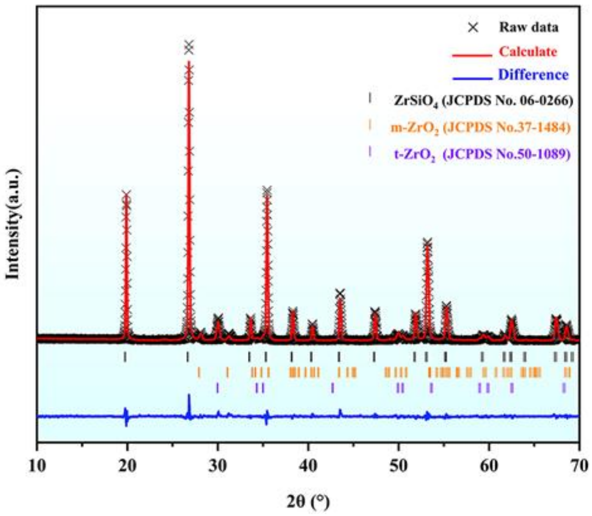

Fig. 10: XRD Rietveld refinement pattern of the pigment sample at F/Zr = 0.3.

Fig. 10 presents the XRD Rietveld refinement pattern of the pigment sample at F/Zr = 0.3, where the fitted pattern shows good agreement with the experimentally measured XRD data. The refinement results are summarized in Table 4. Under these optimized conditions, the content of the main crystalline phase $ZrSiO_4$ reaches 90.39 wt%, which is significantly higher than the 78.94 wt% obtained with 2 mmol NaF (Table 3). Meanwhile, the unit cell parameters (a = b = 6.639 Å, c = 6.002 Å) and unit cell volume (264.55 $Å^3$) increase, indicating a greater incorporation of Pr and Na ions into the crystal lattice. The refinement parameters (χ^2 = 2.04, Rwp = 8.48%, Rp = 6.44%) all fall within acceptable ranges, confirming the reliability of the results.

Fig. 11 shows the FE-SEM images of (Ce, Pr)-$ZrSiO_4$ pigments synthesized at different F/Zr molar ratios (0.1–0.5). At F/Zr = 0.1, the sample primarily exhibits agglomerated amorphous particles, with no well-developed zircon crystals observed. Under this condition, the reaction system failed to overcome the synthesis energy barrier, significantly inhibiting the crystallization process. As the F/Zr molar ratio increases to 0.2–0.4 (Fig. 11(b–d)), the concentration of SiF_4 in the system rises, thereby promoting effective mineralization and vapor-phase mass transfer. During this stage, the crystals follow the inherent anisotropic growth habit of zircon, preferentially growing along the c-axis direction to form typical columnar tetragonal bipyramidal crystals.[33] When the F/Zr ratio further increases to 0.5 (Fig. 11(e)), the crystal morphology transitions from elongated columns to approximately cube-like shapes. This morphological change can be attributed to the rapid crystallization induced by the excessive mineralizer. In this environment, the growth rates in the three dimensions of the crystal tend to balance, ultimately resulting in the development of crystals toward an equiaxed (cube-like) morphology. It is worth noting that at F/Zr = 0.3 (Fig. 11(c)), the crystals exhibit well-developed elongated columnar morphology with clear and intact edges and corners.

To confirm the distribution of each element, EDS elemental mapping was performed on the sample with F/Zr = 0.3, and the results are shown in Fig. 12. It can be clearly observed that the doped elements Ce and Pr both exhibit uniform distribution within the observed area, with no significant elemental segregation or local enrichment detected. These results demonstrate that uniform and stable co-doping of Ce and Pr ions into the $ZrSiO_4$ lattice has been successfully achieved through the mechanochemical-assisted molten salt method combined with the optimized NaF mineralizer.

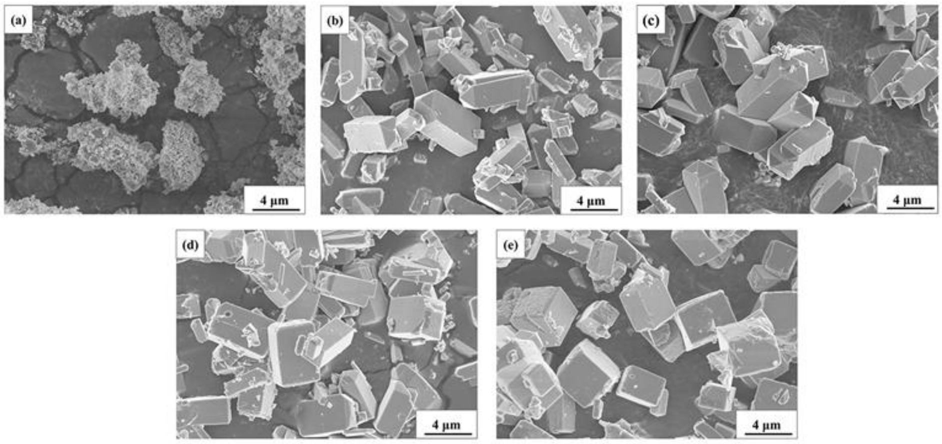

Fig. 11: FE-SEM images of different F/Zr molar ratios samples: (a) 0.1; (b) 0.2; (c) 0.3; (d) 0.4; (e) 0.5.

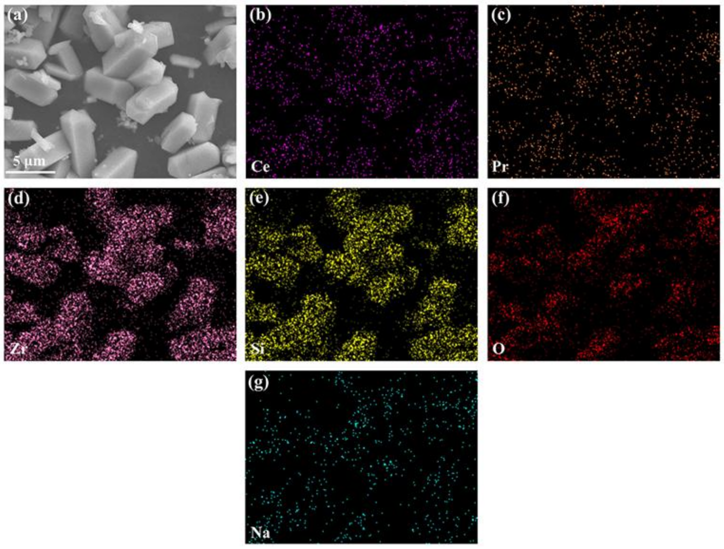

Fig. 12: EDS mapping of sample with F/Zr = 0.3.

The microstructure of the F/Zr = 0.3 sample was further characterized by TEM. As shown in Fig. 13(a), the synthesized pigment particles exhibit well-developed columnar crystals, indicating that the NaF mineralizer effectively regulates the anisotropic growth of $ZrSiO_4$ crystals, consistent with the SEM observations. The HR-TEM image (Fig. 13(e)) displays clear lattice fringes without any lattice mismatch. The measured lattice spacings of 0.330 nm and 0.252 nm correspond to the (020) and $(11\bar{2})$ planes of $ZrSiO_4$ (space group I 4_1/amd).[34] SAED analysis (Fig. 13(d)) further confirms the crystal structure and orientation. The diffraction pattern consists of bright and regularly arranged spots. Indexing of this pattern identifies it as the $ZrSiO_4$ diffraction along the [201] zone axis, with the marked spots corresponding to the (020), $(11\bar{2})$, and $(1\bar{1}\bar{2})$ planes. The SAED results corroborate the HR-TEM observations, jointly confirming the high crystallinity of the product. EDS elemental mapping of a smaller region (Fig. 13(j-m)) also shows uniform distribution of Na along with Zr, Si, O, Pr, and Ce, with no significant local enrichment or segregation observed.

Fig. 14(a) presents the L^*, a^* and b^* values along with digital photographs of pigment samples prepared with varying additions of NaF mineralizer. All pigment samples exhibit a yellow coloration. With increasing addition of the NaF mineralizer, the L^* values of the pigments demonstrate an overall decreasing trend, both a^* and b^* values exhibit an initial increase followed by a subsequent decrease. The highest b^* value (b^* = 68.39) is achieved at an F/Zr = 0.3. Notably, both excessive and insufficient additions of NaF significantly impact the color performance of the pigments. As indicated by the mechanism of the mineralizer action (Eq. (2)), when a low amount of NaF is added, it is entirely consumed in the reaction with SiO_2 to form SiF_4. However, substantial residual SiO_2 remains in the system. This SiO_2 subsequently reacts with ZrO_2 via a mechanism analogous to solid-state synthesis.[2,6] Owing to the relatively low calcination temperature employed (900 °C), which is insufficient for conventional solid-state reaction conditions, the zirconia phase predominates in the resulting pigment at this stage. Nevertheless, the presence of Pr cations enables partial substitution for Zr^{4+} within the zirconia lattice,[35,36] imparting a faint yellow coloration. When a higher amount of NaF is introduced (F/Zr molar ratio exceeding 0.3), the mixture formed with the in situ-generated NaCl exhibits a further lowered melting point.[37] This results in the presence of a significant amount of molten phase within the system. This molten phase readily corrodes the zircon crystals, leading to a reduction in their crystallinity. Consequently, this degradation in crystal structure results in a decrease in the b* value of the pigment. In addition, several related studies also offer an explanation for this phenomenon.[38,39] An excess of mineralizer significantly enhances the synthesis rate of zircon crystals. Consequently, zircon crystals have already formed before Pr cations can substitute for Zr^{4+}. The amount of Pr cations doped into the zircon crystals decreases, thus causing a reduction in the b^* value of the pigment. Correspondingly, it can be seen from the chromatic coordinates (Fig. 14(b)) of the pigment that when the F/Zr is 0.2–0.5, the coordinates of the pigment are closer to the yellow region. When the NaF addition amount is 0.3, the color coordinates change to orange-yellow. Digital photographs of enameled samples incorporating pigments prepared with different NaF additions are presented in Fig. 14(c). Increasing the NaF addition up to 0.3 (F/Zr = 0.3) results in a progressive transition in ceramic glaze color from lemon-yellow to orange-yellow, exhibiting a pronounced warm hue. All enameled sample display smooth surfaces. The prepared zircon based pigments have wide application prospects in the ceramic decoration industry.

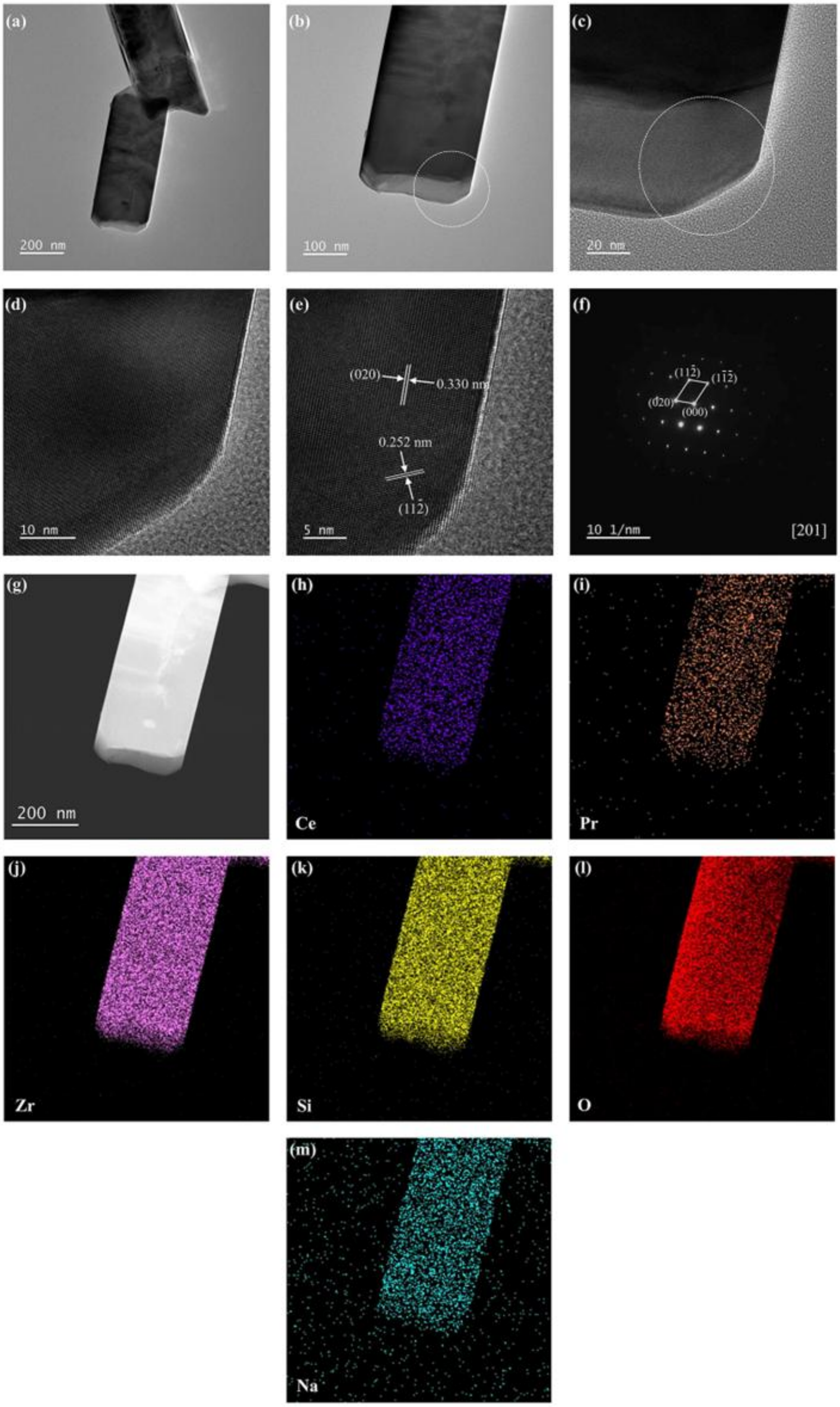

Fig. 13: TEM images, (d-e) HR-TEM image, (f) SAED patterned, (g-m) EDS mapping of sample with F/Zr of 0.3.

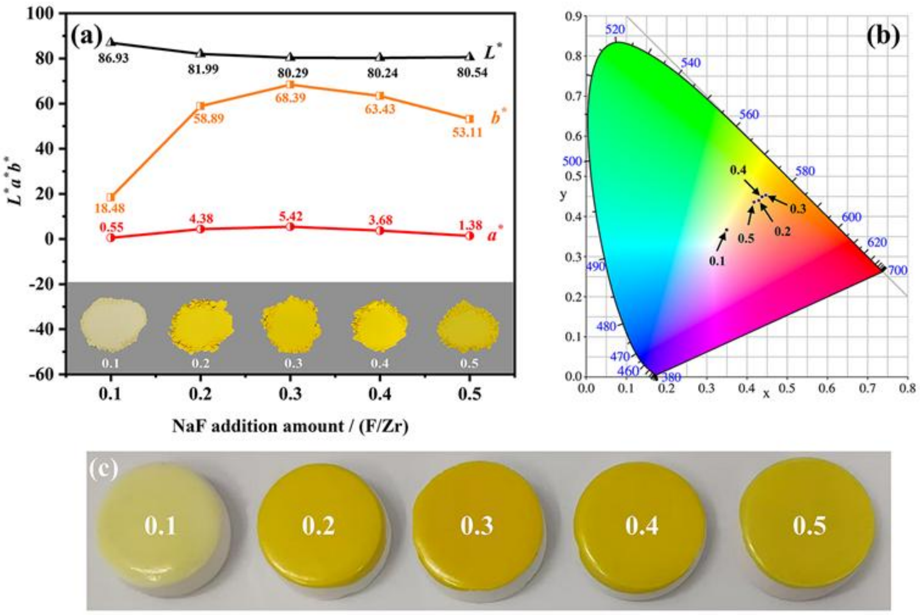

Fig. 14: (a) CIE $L^*a^*b^*$ *values* and digital photographs, (b) chromatic coordinates, (c) photographs of enameled samples of samples with different NaF addition amounts.

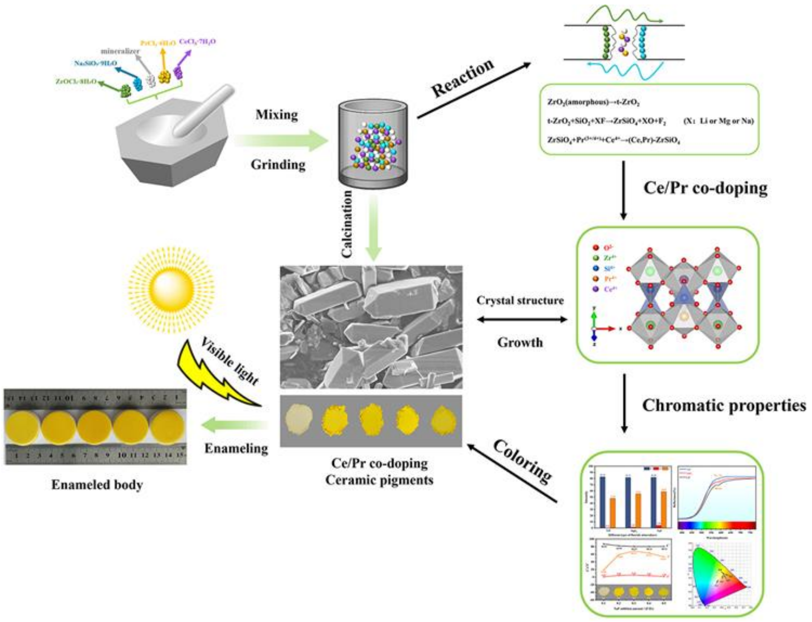

Fig. 15: Schematic diagram of the synthesis and chromogenic mechanism of the (Ce, Pr)-$ZrSiO_4$ pigments.

3.4 Chromogenic mechanism of (Ce, Pr)-$ZrSiO_4$ pigments

Fig. 15 illustrates the chromogenic mechanism of Ce/Pr co-doped $ZrSiO_4$ pigments. The process begins with mechanical grinding, which generates amorphous ZrO_2/SiO_2 precursors and in-situ NaCl molten salt. During calcination, fluoride mineralizers (with NaF being optimal) significantly promote the synthesis of the $ZrSiO_4$ crystalline phase and crystal growth by generating gaseous SiF_4. Simultaneously with crystal formation, Ce and Pr ions are co-incorporated into the $ZrSiO_4$ lattice. XPS analysis confirms that Ce exists stably in the form of Ce^{4+} in the pigments, while Pr coexists in a mixed valence state of Pr^{3+} and Pr^{4+}. The stable high valence state of Ce^{4+} not only modulates the local crystal field environment but also indirectly facilitates the conversion of Pr^{3+} to Pr^{4+}.[40] This study demonstrates that mineralizers are crucial for regulating the valence states of chromogenic ions. Due to its similar ionic radius to Pr^{3+}, Na^+ efficiently compensates for the charge imbalance generated by the substitution of Pr^{3+} for Zr^{4+} through a Pr^{3+}–Na^+ co-occupancy mechanism, creating a stable environment for the$Pr^{3+} \rightarrow Pr^{4+}$ oxidation, thereby significantly increasing the Pr^{4+}/Pr^{3+} ratio. Pr^{4+} as the primary chromogenic center, produces a high-saturation warm yellow color due to an intense and broad absorption band in the blue-violet light region, resulting from charge transfer transitions between O 2p → Pr (IV) 4f orbitals. At an optimal F/Zr molar ratio of 0.3, this synergistic effect is maximized, resulting in excellent color performance (b^* = 68.39).

4. Conclusion

This study prepared (Ce, Pr)-$ZrSiO_4$ yellow ceramic pigments at 900 °C using a mechanochemical-assisted molten salt method, and systematically compared the effects of three fluoride mineralizers (LiF, MgF_2, and NaF) on the phase composition, microstructure, and color performance of the pigments. Preliminary characterization by XRD of the precursors obtained after grinding showed diffraction peaks of NaCl (JCPDS No. 05-0628) in all cases, indicating the in-situ formation of an environmentally friendly and low-cost molten salt medium during the reaction. TG-DTA analysis further revealed the thermal behavior of samples with different mineralizers. The exothermic peaks of the three samples were observed at 632.1 °C (LiF), 673.2 °C (MgF_2), and 667.3 °C (NaF), corresponding to the phase transformation of zirconia and cristobalite; while the endothermic peaks appeared at 763.2 ℃, 790.8 ℃, and 786.1 ℃, respectively, reflecting the melting process of the mixture formed in situ between NaCl and the fluoride mineralizers. The results demonstrate that NaF is significantly superior to LiF and MgF_2 in promoting the formation of the zircon phase, regulating crystal morphology, and enhancing color performance. XPS analysis confirmed that the introduction of NaF resulted in a Pr^{4+}/Pr^{3+} molar ratio of 1.84, substantially higher than the values of 1.19 for the LiF sample and 1.44 for the MgF_2 sample. Furthermore, the NaF sample exhibited the highest reflectance in the yellow wavelength range.

A significant breakthrough of this study lies in the proposal and validation of the Pr^{3+}-Na^+ co-occupancy mechanism. This mechanism reveals that Na^+, due to its similar ionic radius to Pr^{3+}, can co-enter the Zr^{4+} sites withPr^{3+}, effectively compensating for the charge imbalance caused by the substitution of Pr^{3+} for Zr^{4+}. This creates a stable crystal field environment for the conversion of Pr^{3+} to Pr^{4+}. For the remaining unoxidized Pr^{3+} in the system, these Na^+ ions can continue to provide effective charge compensation through the co-occupancy approach. Meanwhile, the study found that different mineralizers have significantly distinct effects on crystal growth behavior. NaF promoted the formation of elongated columnar tetragonal bipyramidal grains with well-defined crystal morphology, sharp edges, and a concentrated and uniform particle size distribution (D_{10} = 0.89 μm, D_{50} = 2.17 μm D_{90} = 4.97 μm). In contrast, LiF and MgF_2 resulted in significant particle agglomeration and the formation of short columnar grains, respectively.

Through systematic optimization of the NaF addition amount, this study identified an F/Zr molar ratio of 0.3 as the optimal process condition. The pigment prepared under this condition not only exhibited the highest phase purity and crystallinity but also demonstrated the optimal chromaticity performance, with color parameters reaching L^* = 80.29, a^* = 5.42, and b^* = 68.39. Further TEM and EDS analyses confirmed the successful achievement of uniform and stable doping of Ce and Pr ions into the $ZrSiO_4$ lattice under these optimized conditions. enameled test results showed that the prepared pigment imparted a highly saturated orange-yellow color to the glaze with a smooth surface, demonstrating excellent coloring ability and decorative effect.

Acknowledgments

This work was supported by the National Natural Science Foundation of China [Grant number: 52362041,52262003]; Natural Science Foundation of Jiangxi Province [Grant number. 20242BAB20166, 20232ACB204012, 20232BAB204031]; Jiangxi Province Major Discipline Academic Technology Leader Training Program [Grant number: 20243BCE51117].

Conflict of Interest

There is no conflict of interest.

Supporting Information

Not applicable.

CRediT Statement

Feng Jiang: Conceptualization, Methodology, Writing – Review and editing, Funding acquisition. **Jie Liu:** Investigation, Writing – Original draft, Data curation, Formal analysis. **Junxiong Zhang:** Software, Formal analysis. **Zhibin Chen:** Writing – Original draft. **Guo Feng:** Writing – Review and editing, Resources, Funding acquisition. **Quan Zhang:** Writing – review and editing. **Xiaojun Zhang:** Supervision, Funding acquisition. **Jianmin Liu:** Writing – Review and editing, Funding acquisition.

References

[1] E. Snyders, J. H. Potgieter, J. T. Nel, The effect of milling and percentage dissociation of plasma dissociated zircon on the colour of Pr-yellow and V-blue zircon pigments, *Journal of the European Ceramic Society*, 2006, **26**, 1599-1603, doi: 10.1016/j.jeurceramsoc.2005.03.237.

[2] X. He, F. Wang, H. Liu, J. Li, L. Niu, Synthesis and coloration of highly dispersed NiTiO 3 @TiO 2 yellow pigments with core-shell structure, *Journal of the European Ceramic Society*, 2017, **37**, 2965-2972, doi: 10.1016/j.jeurceramsoc.2017.03.020.

[3] Sikalidis, C. (Ed.). Advances in Ceramics - Synthesis and Characterization, *Processing and Specific Applications*, Rijeka: InTech, 2011, 75-100, ISBN: 978-9533075051.

[4] C. E. Curtis, H. G. Sowman, Investigation of the thermal dissociation, reassociation, and synthesis of zircon, *Journal of the American Ceramic Society*, 1953, **36**, 190-198, doi: 10.1111/j.1151-2916.1953.tb12865.x.

[5] W. H. Jiang, Y. H. Yang, Q. X. Zhu, J. M. Liu, Iron-zircon pigments prepared by non-hydrolytic Sol-gel method at low temperature, *Advanced Materials Research*, 2011, **412**, 223-226,

doi: 10.4028/www.scientific.net/amr.412.223.

[6] C. Cai, Y. Wu, J. Wei, J. Zhang, Y. Zhang, High near-infrared reflectance $Zn_{1-x}Mn_xO$ yellow pigment prepared and properties by co-precipitation method, *Materials Today Communications*, 2024, **41**, 110403, doi: 10.1016/j.mtcomm.2024.110403.

[7] V. V. Boldyrev, K. Tkáčová, Mechanochemistry of solids: past, present, and prospects, *Journal of Materials Synthesis and Processing*, 2000, **8**, 121-132, doi: 10.1023/A:1011347706721.

[8] J. A. Badenes, J. B. Vicent, M. Llusar, M. A. Tena, G. Monr, The nature of Pr-$ZrSiO_4$ yellow ceramic pigment, *Journal of Materials Science*, 2002, **37**, 1413-1420, doi: 10.1023/A:1014537000690.

[9] D.N. Giulia, C. Giuseppe, A. Silvia, F. Paola, G. Stefania, Yellow Pr-zircon pigments: The role of praseodymium and of the mineralizer, *Journal of the American Ceramic Society*, 2004, **24**, 3603-3611, doi: 10.1016/j.jeurceramsoc.2004.01.003.

[10] N. Masó, H. Beltrán, R. Muñoz, B. Julián, J. B. Carda, P. Escribano, E. Cordoncillo, Optimization of praseodymium-doped cerium pigment synthesis temperature, *Journal of the American Ceramic Society*, 2003, **86**, 425-430, doi: 10.1111/j.1151-2916.2003.tb03316.x.

[11] J. Yu, F. Jiang, W. Jin, X. Zhang, Q. Zhang, R. Zhang, Q. Wu, Y. Yu, T. Xu, G. Feng, Mineralizer and charge-compensator synergistically enhanced novel (Li, Cr)–$ZrSiO_4$ jade green pigment and its near-infrared reflection performance, *Ceramics International*, 2024, **50**, 15709-15719, doi: 10.1016/j.ceramint.2024.02.051.

[12] S. Peng, R. Yang, B. Lei, R. Chen, Y. Gao, X. Xia, K. P. Homewood, New insight into the coloration mechanism and synthesis of ultrafine Pr-$ZrSiO_4$ yellow pigments, *Journal of the American Ceramic Society*, 2023, **106**, 5476-5486, doi: 10.1111/jace.19150.

[13] R. D. Shannon, Revised effective ionic radii and systematic studies of interatomic distances in halides and chalcogenides, *Acta Crystallographica Section A*, 1976, **32**, 751-767, doi: 10.1107/s0567739476001551.

[14] B. H. Toby, *EXPGUI*, a graphical user interface for*GSAS*, *Journal of Applied Crystallography*, 2001, **34**, 210-213, doi: 10.1107/s0021889801002242.

[15] J. Yu, F. Jiang, J. Liu, T. Wang, X. Zhang, Q. Zhang, R. Zhang, Q. Wu, Q. Hu, Y. Yu, G. Feng, Coloring and near-infrared reflection performance of low-temperature synthesized novel (Cr, V)–$ZrSiO_4$ jewel green pigments, *Ceramics International*, 2023, **49**, 38602-38613, doi: 10.1016/j.ceramint.2023.09.193.

[16] M. Llusar, J. B. Vicent, J. Badenes, M. A. Tena, G. Monrós, Environmental optimisation of blue vanadium zircon ceramic pigment, *Journal of the European Ceramic Society*, 1999, **19**, 2647-2657, doi: 10.1016/s0955-2219(99)00041-2.

[17] J. Yu, F. Jiang, G. Feng, T. Wang, X. Zhang, J. Liu, Q. Zhang, Q. Wu, Y. Yu, Sensitization and mineralization synergistically enhanced the coloration of V to Cr-doping $ZrSiO_4$ based jewel green pigment and its near-infrared reflection performance, *Ceramics International*, 2024, **50**, 38688-38697, doi: 10.1016/j.ceramint.2024.07.240.

[18] H. M. Haendler, P. S. Sennett, C. M. Wheeler, The system LiF-LiCl, LiF-NaCl, LiF-KCl, *Journal of the Electrochemical Society*, 1959, **106**, 264, doi: 10.1149/1.2427319.

[19] R. A. Sharma, I. Johnson, Phase diagrams for the systems $MgCl_2$-MgF_2, $CaCl_2$-MgF_2, and NaCl-MgF_2, *Journal of the American Ceramic Society*, 1969, **52**, 612-615, doi: 10.1111/j.1151-2916.1969.tb15851.x.

[20] C. E. Johnson, E. J. Hathaway, Solid-liquid phase equilibria for the ternary systems Li(F, Cl, I) and Na(F, Cl, I), *Journal of the Electrochemical Society*, 1971, **118**, 631, doi: 10.1149/1.2408125.

[21] M. Ocaña, A. Caballero, A. R. González-Elipe, P. Tartaj, C. J. Serna, R. I. Merino, The effects of the NaF flux on the oxidation state and localisation of praseodymium in Pr-doped zircon pigments, *Journal of the European Ceramic Society*, 1999, **19**, 641-648, doi: 10.1016/s0955-2219(98)00233-7.

[22] R. A. Eppler, Mechanism of formation of zircon stains, *Journal of the American Ceramic Society*, 1970, **53**, 457-462, doi: 10.1111/j.1151-2916.1970.tb12677.x.

[23] D. N. Kamaev, S. A. Archugov, G. G. Mikhailov, Study and thermodynamic analysis of the ZrO_2-SiO_2 system, *Russian Journal of Applied Chemistry*, 2005, **78**, 200-203, doi: 10.1007/s11167-005-0259-2.

[24] G. Peev, T. Racheva, E. Dacheva, N. Nedev, Thermal oxidation of silicon in $O_2^-SiF_4$ mixtures, *Thin Solid Films*, 1989, **169**, 173-178, doi: 10.1016/s0040-6090(89)80015-x.

[25] J.A. Dean, *Lange's handbook of chemistry*, New York, McGraw Hill, Fifteenth Edition, 1998, ISBN: 978-0070163843.

[26] G. Lanaro, G. N. Patey, The influence of ion hydration on nucleation and growth of LiF crystals in aqueous solution, *The Journal of Chemical Physics*, 2018, **148**, 024507, doi: 10.1063/1.5001521.

[27] J. Liu, T. Wang, Q. Gao, W. Jiang, L. Miao, G. Feng, F. Jiang, Effect of NaF content on the preparation of zirconia whiskers by molten salt method, *Advanced Powder Technology*, 2021, **32**, 998-1003, doi: 10.1016/j.apt.2021.02.006.

[28] M. Baron, O. Bondarchuk, D. Stacchiola, S. Shaikhutdinov, H.-J. Freund, Interaction of gold with cerium oxide supports: CeO_2(111) thin films vs CeO_x nanoparticles, *The Journal of Physical Chemistry C*, 2009, **113**, 6042-6049, doi: 10.1021/jp9001753.

[29] T. Chen, J. Zha, X. Zhang, X. Hu, W. Jiang, Z. Xie, W. Jiang, Synthesis and characterization of $Pr_xZr_{1-x}SiO4$ (x = 0–0.08) yellow pigments *via* non-hydrolytic Sol-gel method, *Journal of the European Ceramic Society*, 2018, **38**, 4568-4575, doi:

10.1016/j.jeurceramsoc.2018.05.021.

[30] X.-L. Yang, X.-X. Wan, Analysis of the spectral reflectance and color of mineral pigments affected by their particle size, *Color Research & Application*, 2020, **45**, 246-261, doi: 10.1002/col.22455.

[31] Y. Wang, F. Lai, Q. Wang, Q. Long, C. Wang, W. Zhang, Q. Chang, Synthesis and chromatic properties of high color performance Prx-$ZrSiO_4$ (x = 0–0.1) yellow pigment, *Journal of Alloys and Compounds*, 2022, **891**, 161932, doi: 10.1016/j.jallcom.2021.161932.

[32] C. G. Pope, X-ray diffraction and the Bragg equation, *Journal of Chemical Education*, 1997, **74**, 129, doi: 10.1021/ed074p129.

[33] Z.K. W, *Whisker Materials: Technology and Applications*, Shanghai, Shanghai Jiaotong University Press, 2022, ISBN: 978-7313263339.

[34] T. Kittiauchawal, A. Mungchamnankit, S. Sujinnapram, J. Kaewkhao, P. Limsuwan, The effect of heat treatment on crystal structure in zircon monitored by ESR and XRD, *Procedia Engineering*, 2012, **32**, 706-713, doi: 10.1016/j.proeng.2012.02.001.

[35] S. P. Radhika, K. J. Sreeram, B. U. Nair, Rare earth doped cobalt aluminate blue as an environmentally benign colorant, *Journal of Advanced Ceramics*, 2012, **1**, 301-309, doi: 10.1007/s40145-012-0029-6.

[36] F. Tabatabaian, Color in zirconia-based restorations and related factors: a literature review, *Journal of Prosthodontics*, 2018, **27**, 201-211, doi: 10.1111/jopr.12740.

[37] J. Sangster, A. D. Pelton, Phase diagrams and thermodynamic properties of the 70 binary alkali halide systems having common ions, *Journal of Physical and Chemical Reference Data*, 1987, **16**, 509-561, doi: 10.1063/1.555803.

[38] M. Llusar, J. A. Badenes, J. Calbo, M. A. Tena, G. Monrós, Environmental and colour optimisation of mineraliser addition in synthesis of iron zircon ceramic pigment, *British Ceramic Transactions*, 2000, **99**, 14-22, doi: 10.1179/bct.2000.99.1.14.

[39] O. V. Merkulov, A. A. Markov, N. S. Uporova, D. A. Zamyatin, Investigation into the significant effect of CuO additive on the synthesis of $ZrSiO_4$: phase formation and crystallization at low temperature, *Journal of Thermal Analysis and Calorimetry*, 2022, **147**, 11747-11757, doi: 10.1007/s10973-022-11387-4.

[40] D. Guo, M. Xie, N. Ma, Q. Yang, Z. Luo, Y. Chu, Y. Zhang, P. Rao, Synthesis and characterization of (Pr, Ce)-$ZrSiO_4$ ceramic pigments: the properties of the pigments and the effect of Ce, *Journal of the American Ceramic Society*, 2019, **102**, 2619-2628, doi: 10.1111/jace.16112.

Open Access